



Article

A Hidden Eruption: The 21 May 2023 Paroxysm of the Etna Volcano (Italy)

Emanuela De Beni ¹, Cristina Proietti ^{1,*}, Simona Scollo ¹, Massimo Cantarero ¹, Luigi Mereu ^{2,3}, Francesco Romeo ^{1,3,4}, Laura Pioli ⁵, Mariangela Sciotto ¹ and Salvatore Alparone ¹

- ¹ Istituto Nazionale di Geofisica e Vulcanologia, Osservatorio Etneo, 95125 Catania, Italy; emanuela.debeni@ingv.it (E.D.B.); simona.scollo@ingv.it (S.S.); massimo.cantarero@ingv.it (M.C.); francesco.romeo@ingv.it (F.R.); mariangela.sciotto@ingv.it (M.S.); salvatore.alparone@ingv.it (S.A.)
- ² Istituto Nazionale di Geofisica e Vulcanologia, Sezione di Bologna, 40127 Bologna, Italy; luigi.mereu@ingv.it
- ³ Centre of Excellence CETEMPS, University of L'Aquila, 67100 L'Aquila, Italy
- ⁴ Department of Information Engineering, Electronics, and Telecommunications, Sapienza University of Rome, 00185 Rome, Italy
- ⁵ Dipartimento di Scienze Chimiche e Geologiche, Università degli Studi di Cagliari, 09124 Cagliari, Italy; laura.pioli@unica.it
- * Correspondence: cristina.proietti@ingv.it

Abstract: On 21 May 2023, a hidden eruption occurred at the Southeast Crater (SEC) of Etna (Italy); indeed, bad weather prevented its direct and remote observation. Tephra fell toward the southwest, and two lava flows propagated along the SEC's southern and eastern flanks. The monitoring system of the Istituto Nazionale di Geofisica e Vulcanologia testified to its occurrence. We analyzed the seismic and infrasound signals to constrain the temporal evolution of the fountain, which lasted about 5 h. We finally reached Etna's summit two weeks later and found an unexpected pyroclastic density current (PDC) deposit covering the southern lava flow at its middle portion. We performed unoccupied aerial system and field surveys to reconstruct in 3D the SEC, lava flows, and PDC deposits and to collect some samples. The data allowed for detailed mapping, quantification, and characterization of the products. The resulting lava flows and PDC deposit volumes were $(1.54 \pm 0.47) \times 10^6 \text{ m}^3$ and $(1.30 \pm 0.26) \times 10^5 \text{ m}^3$, respectively. We also analyzed ground-radar and satellite data to evaluate that the plume height ranges between 10 and 15 km. This work is a comprehensive analysis of the fieldwork, UAS, volcanic tremor, infrasound, radar, and satellite data. Our results increase awareness of the volcanic activity and potential dangers for visitors to Etna's summit area.

Keywords: remote sensing monitoring system; Etna paroxysm; pyroclastic density current; UAS survey; fieldwork; volcanic tremor; infrasound



Citation: De Beni, E.; Proietti, C.; Scollo, S.; Cantarero, M.; Mereu, L.; Romeo, F.; Pioli, L.; Sciotto, M.; Alparone, S. A Hidden Eruption: The 21 May 2023 Paroxysm of the Etna Volcano (Italy). *Remote Sens.* **2024**, *16*, 1555. <https://doi.org/10.3390/rs16091555>

Academic Editors: **Ciro Del Negro** and **Jonathan Procter**

Received: 7 March 2024

Revised: 11 April 2024

Accepted: 23 April 2024

Published: 27 April 2024



Copyright: © 2024 by the authors. Licensee MDPI, Basel, Switzerland. This article is an open access article distributed under the terms and conditions of the Creative Commons Attribution (CC BY) license (<https://creativecommons.org/licenses/by/4.0/>).

1. Introduction

Volcano monitoring is a process that involves collecting and analyzing, in real-time, a large volume of data to track the behavior of a volcano, identify any signs of unrest, provide short-term forecasts for potential eruptions, and mitigate the potential risks. Seismic, infrasound, geodetic, geochemical, topographic, radar, and geological data, along with fieldwork and knowledge of the past volcanic behavior have a fundamental role in observing and understanding ongoing processes within active volcanic systems [1]. The key methods for monitoring an eruption and quantifying its products include (i) ground-based observation, (ii) analyses of terrestrial, drone, aerial, and satellite imagery, (iii) sample collection for petrochemical analyses, and (iv) temperature measurements [1–4].

Volcanic tremor provides valuable insights into the upward migration of magma and gas in the plumbing system [5–9]. Its variations over time are useful for investigating the temporal evolution of explosive eruptions, e.g., [10–12], and to understand the physical

processes underlying them [13]. The amplitude of volcanic tremor correlates closely with the intensity of explosive activity. Specifically, it gradually increases during the activity ramp-up that leads to a lava fountain, reaching its peak at the eruption climax, and then it rapidly decreases to a pre-eruption level at the end of a paroxysm [14–20].

Infrasonic signals are generated by magma and fluid dynamics occurring at the interface with the atmosphere. Its analysis is complementary to that of volcanic tremor and plays an important role in volcano monitoring. It was revealed to be useful both for monitoring purposes and for the characterization of explosive activity [21–23].

Surficial mass movements such as pyroclastic density currents (PDCs) can generate seismic and infrasound signals in volcanic areas. However, PDCs often occur during eruptions; thus, pinpointing their trace on seismic and infrasound signals has proved to be a demanding task [24]. Although there have been several attempts to link volcanic tremor to an explosive activity [25], general procedures do not exist yet because the volcanic tremor is also linked to the magma intrusion and oscillations of the magma in the conduit [26]. Instead, new methodologies are available for infrasound signal analysis, which have been recently used to estimate the mass/volume emission rate [27,28].

Ground-based microwave radars at S, C, and X bands represent an important tool for detecting volcanic ash clouds in all weather conditions at a fairly high space–time resolution [29].

Satellite data are useful to estimate the volcanic plume’s altitude. The global perspective offered by Meteosat Second Generation (MSG) geostationary satellite does not allow discrimination between the meteorological cloud and the volcanic plume due to the poor spatial resolution of the SEVIRI sensor (approximately 3 km), mostly when coupled with bad weather conditions [30]. By contrast, if the scene is observed with a low earth orbit (LEO) satellite, such as Sentinel 3-A, it is possible to identify the plume due to the higher spatial resolution of the sensors on board [31].

Unoccupied aerial systems (UASs) are useful tools for volcano monitoring that allow observation from above. The acquired visible and thermal images, which are processed through the structure from motion (SfM) technique to extract orthomosaics (OMs) and through the digital elevation model (DEM), are essential to map and quantify the volcanic products and features [32].

Three of the world’s most active volcanoes, Piton de la Fournaise, the Hawaiian volcanoes, and Etna, are closely monitored through networks of multi-parametric sensors. Piton de la Fournaise is a basaltic hotspot volcano located on La Réunion (a French island in the Indian Ocean) that erupts, on average, twice a year. Its 2022 lava flow has been monitored and quantified by aerial photogrammetry and multiple satellite sensors [33]. The six Hawaiian shield volcanoes are the largest and most active volcanoes on Earth and are characterized by lava fountains, Strombolian activity, and lava lakes and flows [34]. The 2014–2015 Pāhoā crisis on the island of Hawai’i was monitored through a UAS [35]. Moreover, the Mauna Loa 2022 eruption was monitored from space, integrating the information from different satellite sensors [36].

Etna is a basaltic stratovolcano located along the Ionian coast of eastern Sicily (Italy). For millennia, people have been fascinated by this volcano and have coexisted with it; indeed, one million people still live on its flanks. Etna is characterized by effusive and moderate explosive activity that frequently occurs from its four summit craters (Figure 1): Voragine (VOR), the Northeast Crater (NEC), Bocca Nuova (BN), and the Southeast Crater (SEC). Lateral eruptions occur less often from Etna’s flanks. Explosive activity, from both the summit and the flanks, is often associated with lava flows and includes lava fountains and Strombolian explosions, which are responsible for the growth of scoria cones [37]. The most powerful explosive events from Etna’s summit craters are called paroxysms. They produce violent Strombolian activity or pulsating to sustained lava fountains, which form eruptive columns of ash, lapilli, and gas, rising to about 15 km above sea level [3,38]. Paroxysms generally feed fast-moving and short-lasting lava flows that extend a few kilometers from the summit [14]. Several high-magnitude events have been recorded at Etna’s summit

craters since 1900, and their frequency has increased since the 1970s [39]. Since 2000, most of them have occurred at the SEC, which was formed in 1971 and is currently the most active of the four summit craters and the highest point on Etna. On 16 September 2021, its maximum altitude was 3348 ± 1 m a.s.l., as measured by UAS surveys [40].

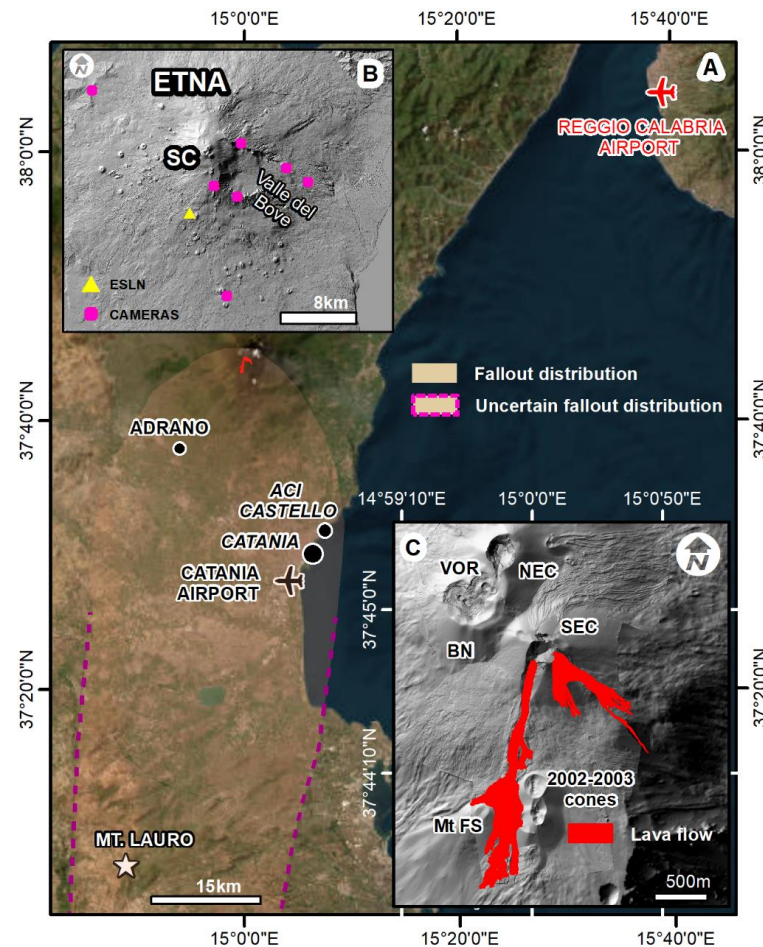


Figure 1. (A) Eastern Sicily, showing the airports, radar locations (star close to Mt. Lauro = Monte Lauro; Catania and Reggio Calabria airports), lava flows, and fallout distribution of the 21 May 2023 eruption. Base map: Esri, Maxar, Earthstar Geographics; (B) Location of Etna's camera network and ESLN (Serra La Nave) seismic and infrasonic station; SC = summit craters; (C) Etna's summit area and the 21 May 2023 lava flows (NEC = Northeast Crater, VOR = Voragine crater; BN = Bocca Nuova crater, SEC = Southeast Crater; Mt FS = Mount Frumento Supino). The background images in B and C are a shaded relief from [40].

Although Etna's lava flows may not pose an immediate threat to human life, it is important to note that they can trigger dangerous and localized phreatic explosions when they come into contact with snow or water [41–43]. Explosive activities can cause several hazards. High eruptive columns rise to the top of the troposphere, and volcanic ash can be dispersed up to several hundreds of kilometers [44] and disrupt aviation operations [45]. At the same time, tephra fallout can impact infrastructures, crops, vegetation [46], and human health [47]. Moreover, the fallout of large clasts (>5 cm) and ballistics can affect the proximal and medial areas and cause injury to people [15,48–50]. Small-volume ($<2 \times 10^6$ m³) pyroclastic density currents (PDCs) may also be produced during or after a paroxysm [51–54]. PDCs can be due to (1) the collapse of pyroclastic fountains; (2) the failure and/or sliding of pyroclastic deposits emplaced on steep slopes during intense lava fountaining; (3) the gravitational collapse of lava flow fronts; or (4) the lava interaction/mixing with of wet rocks or snow [53].

Due to its multi-hazardous nature and its proximity to people, Etna is monitored by the Istituto Nazionale di Geofisica e Vulcanologia, Osservatorio Etneo (INGV-OE) through a network of multi-parametric sensors whose signals are conveyed, in almost real-time, to the control room. In particular, eruptive activity is observed through a network of surveillance, visible, and thermal cameras [55] and three ground-based radars [56] located at the Catania and Reggio Calabria airports and at Monte Lauro (Figure 1). The seismicity and infrasound signals are monitored through permanent seismic and infrasonic networks. The former currently consists of about 30 digital broadband 3-component stations and the second one of 10 sensors co-located with the seismic ones [23,57]. The strain changes related to the SEC's lava fountains are measured through four borehole dilatometers [58].

This paper details a hidden eruption that occurred at Etna's SEC on 21 May 2023. This event is considered hidden because it was not directly or remotely observed due to bad weather conditions. The occurrence of volcanic unrest was highlighted by abrupt changes in volcanic tremor, infrasound signals, deformation, and tephra fallout. The eruption produced a lava fountain and two lava flows, one of which was partially covered by a PDC deposit. This research aims to reconstruct and quantify this yet uninvestigated eruption by analyzing various sources of data such as seismic and infrasound signals, remote sensing data from UASs, radars, and satellites, and fieldwork data. The reconstruction also aims to confirm the hypothesis that the PDC is coeval with the lava flow, as suggested by ground observations. Our analysis distinguishes the main phases of the eruption, even if the time of PDC occurrence is not identifiable. It quantifies the height of the plume, the lava flows, and the PDC deposit. Our findings have the potential to improve the knowledge and monitoring of Etna's summit eruptions, particularly of minor PDCs from the SEC.

The 21 May 2023 Eruption

Since there is no direct or remote observation of the 21 May 2023 eruption, its occurrence, as well as its start and end times, were derived only from the analysis of seismic, infrasound, and deformation signals recorded by INGV monitoring networks [59]. Strombolian activity at the SEC resumed on the 4 of May at 10:10 UTC (hereafter, all times are in UTC). On 18 May, a sudden increase in the average root mean square (RMS) of the tremor was recorded, with its source below the SEC. On 21 May at 5:20, a further increase in the tremor RMS and infrasonic events (number and amplitude) marked the onset of a lava fountain. The lava fountain, lasting at least 4 h, formed a plume of about 10 km, the ash of which fell along the southwest flank (i.e., Adrano) and later, due to a slow change in wind direction, from the southern to the southeastern sector (i.e., from Catania to Aci Castello; Figure 1). A lava flow from the southernmost vent propagated along the southern flank and passed between the 2002–2003 scoria cones and Mt. Frumento Supino (Mt. FS), and another flow formed along the SEC's eastern flank (Figure 1). The volcanic tremor abruptly returned to its background value at around 09:40, thus indicating the end of the event [59]. Adverse weather conditions, with severe thunderstorms, dense cloud cover over Etna's summit, and abnormal (for May) snow cover, persisted for two weeks after the eruption ended. This situation hindered both direct field surveys and remote sensing analysis of the erupted product.

2. Materials and Methods

To describe and quantify the 21 May 2023 eruption at Etna, we combined different monitoring data: the volcanic tremor and infrasound signals, acquired by the permanent networks; the signals recorded by three ground-based radars, satellite data, several UAS-acquired images; and field data.

2.1. Volcanic Tremor and Infrasound Signals

To track the amplitude changes in volcanic tremor on 21 May 2023, we calculated the RMS of the seismic (vertical component) and infrasound signals recorded by the Serra La Nave (ESLN) station of INGV-OE, located on the southern flank, 6.5 km from the SEC

(Figure 1). ESLN is equipped with a broadband three-component Trillium seismometer (40s cut-off period; Nanometrics™ 3001 Solandt Rd, Kanata, Canada), with a sampling rate of 100 Hz. ESLN also has a polarized free-field low-frequency microphone (G.R.A.S. 40 AN [60]; flat response between 0.3 Hz and 20 kHz (+/− 2 dB)) with a sampling rate of 50 Hz and a sensitivity of 50 mV/Pa. The RMS time series were calculated for 1-min-long time windows for both signals. To minimize the noise due to the wind, the infrasound signal above 0.3 Hz was filtered. A visual inspection of seismic and infrasound signals was also carried out to identify potential signals associated with the PDC [61].

2.2. Radar Signals

To characterize the 21 May 2023 explosive activity and to measure the top plume height, we analyzed the signals registered by three ground-based radars (Figure 1): two X-band radars, located at the Vincenzo Bellini airport (Catania, Sicily) and Reggio Calabria airport (Reggio Calabria, Calabria), and one C-band radar located in Monte Lauro (Siracusa, Sicily). To focus our analysis only on the eruption column, we singled out an area of about 20 km × 20 km centered around Etna's summit area, where we observed the maximum variability in the radar reflectivity factor Z_h . The radar signal we processed is Z_h , which generally has a variability between 60 dBZ (in correspondence with the paroxysmal phase) and a few dBZ (mainly at the beginning and end of explosive activity). It was appropriately filtered and corrected to highlight the volcanic signature better. Applying the volcanic-ash radar retrieval (VARR) method to radar measurements [56,62,63], we can: (1) classify the tephra class using the maximum a posteriori (MAP) probability criterion; and (2) estimate the main tephra features, such as the tephra concentration C_t (g/m³) and the mean diameter D_n (mm) of tephra particles. Using a threshold algorithm on the measured Z_h , we can estimate the top plume height (H_{TP}) above sea level (km a.s.l.) and the associated uncertainty of ± 300 m [56,64,65]. We retrieved the wind velocity v_W (m/s), averaged between the estimated H_{TP} and the Etna summit (3348 m a.s.l.), by processing the wind velocity profiles from the freely available ERA5 reanalysis of the European Centre for Medium-Range Weather Forecasts (ECMWF) [66]. Knowing the H_{TP} and v_W , we can characterize this eruptive event by evaluating the time variation in the mass eruption rate MER (kg/s) through the one-dimensional empirical model of Degruyter and Bonadonna, hereinafter DB12 [64,67,68].

2.3. Satellite Data

To estimate the altitude of the 21 May 2023 plume (measured in km a.s.l.) in the proximity of the vent, we coupled Sentinel-3A data, acquired through the Ocean and Land Color Instrument (OLCI), with the atmospheric profile. OLCI collects spectral radiances (mW m^{−2} sr^{−1} nm^{−1}) in 21 bands distributed in the visible (VIS) and near-infrared spectral regions [69]. We also use the Sea and Land Surface Temperature Radiometer (SLSTR), which collects spectral radiances in 11 bands from the VIS to thermal-infrared (TIR) regions [70]. The pre-processed data (L1B products) were downloaded from the EUMETSAT data store [71] in the .netCDF format. The OLCI data were downloaded at full resolution (i.e., 300 m), whereas the SLSTR data were at 0.5 km and 1.0 km for VIS and TIR, respectively. The atmospheric data were downloaded from the ECMWF data provider [66]. The plume altitude is estimated using the well-assessed coldest-pixel method [72]. The lowest brightness temperature (BT) in the plume is compared with the temperature gradient measured in proximity to the volcano. We defined an area of ≈3.0 km², centered over Etna, and we selected the coldest pixel observed at 10.85 μm, the channel sensitive to silicate particles [31]. We evaluated the brightness temperature difference (BTD) between two channel windows: 8–11 μm and 12–14 μm. Silicate particles absorb more in the 8–11 μm window, whereas water particles absorb more in the 12–14 μm window. A high concentration of water particles results in a positive difference, while a high concentration of ash particles results in a negative difference.

2.4. UAS-Acquired Images

To observe, document, and map the 21 May 2023 erupted products and to update the topography, on 27 May, we performed a first-field and UAS survey of the area affected by the eruption, with a DJI Phantom 4 Pro RTK and a DJI Mavic Enterprise 2. This survey was useful for providing initial observations, but it was not suitable for photogrammetry, because the SEC summit was hindered by clouds and gas. The ground observation allowed the identification of a reddish volcanoclastic deposit, probably produced by a PDC that was deposited on the south lava flow. The adverse weather conditions and the great amount of gas necessitated two more UAS surveys, on the 9 and 23 of June, to cover the entire area affected by the eruption (Table 1).

Table 1. The most important information about each flight. Date of the surveys and the UAS utilized; GOAL is the main purpose; OBS. = Observation; PHOT. = Photogrammetry; ID identifies the flights; n° indicates the number of images, and videos taken during each flight; and altitude is the range of the UAS.

Survey Date	UAS Type	Goal	ID	Image n°	Video n°	Altitude Range (m)
27 May 2023	DJI PH4 RTK	OBS.	1	151	2	3015–3376
	DJI MAVIC 2		2	164	5	
			3	85	2	
9 June 2023	DJI PH4 RTK	PHOT.	1	221	0	2978–3156
			2	85	0	
			1	280	1	
23 June 2023	DJI PH4 RTK	PHOT.	2	283	2	2693–3381
			3	282	5	
			4	350	0	
	DJI MAVIC 2	OBS.	5	410	0	

To ensure optimal results from the photogrammetric processing, we carefully selected the best images acquired during the two PHOT. surveys, performed with the DJI PH4 RTK, by eliminating blurry, redundant, or overcast photos. We processed the selected UAS images through the Agisoft Metashape (Version 1.6.6) structure-from-motion photogrammetric software [73]. From both surveys, we extracted the digital terrain models (DTMs) and orthomosaics (OMs). In particular, the products from the 9 June survey covered the southern lava flow, the PDC, and, partially, the SEC, with resolutions of 31.5 and 7.9 cm/px for the DTM and OM, respectively. The 23 June survey was performed to cover the rest of the SEC, and it resulted in a DTM and an OM with resolutions of 17.4 and 8.7 cm/px, respectively (Table 2). Unfortunately, UAS images of the eastern flow were inadequate for properly performing the photogrammetric process.

Table 2. The most important information about the processing, i.e., survey date, number of processed images, and alignment quality, and about the output products, i.e., number of points in the dense clouds, spatial resolution of the digital terrain models (DTM) and orthomosaics (OMs).

Survey Date	n° of Processed Images	Alignment Quality	n° of Points of the Dense Cloud	DTM Resolution (cm/px)	OM Resolution (cm/px)
9 June 2023	164	high	13975781	31.5	7.9
23 June 2023	191	high	21032118	17.4	8.7

To compare topographic datasets extracted at different dates, we reduced the misalignment errors by performing manual and automatic alignment through the Cloud Compare (Version 2.12.4) open-source software [74]. This processing was first performed between the two post-eruption point clouds (9 and 23 June), which were merged after alignment. Then, the merged post-eruption point cloud was resampled at 50 cm and aligned with a pre-eruption one extracted from the 19 October 2022 UAS survey (DTM with a resolution

of 50 cm/px). The aligned post-eruption and pre-eruption clouds were converted into two DTMs using the Cloud Compare software (Version 2.12.4). The reference system of all the analyzed data is the World Geodetic System 1984 (WGS84), and all the elevations measured in this work are ellipsoidal; to obtain the geoidic elevation, subtract 42 m.

Accurate mapping and quantification of the volcanic products (i.e., measurements of their length, minimum elevation, area, thickness, and volume) were performed by analyzing, through the ESRI ArcGIS Desktop (Version 10.6.1) software, the pre- and post-eruption DTMs and the post-eruption orthomosaics [40]. In particular, the southern lava flow and the pyroclastic deposit were delimited on the post-eruption OM. It was also used to check the positioning of the samples collected in the field. Since we did not have an OM depicting the eastern flow, we drew its map by analyzing a few visible and thermal images. The post- and pre-eruption DTMs were compared through the topographic approach, which calculates the elevation differences between datasets acquired on different dates [75]. The standard deviation between the two DTMs, calculated where no natural changes occurred, is a useful measure of the error associated with the alignment of the two dense clouds, pre- and post-eruption [76]. It was calculated over a total area of 230,609 m² and gave a result of 20 cm. We measured the cumulative thickness of the lava and PDC deposits by extracting DTM elevation differences within the limits of the southern lava flow. To calculate the corresponding volume, we summed, over all the pixels, the volume accumulated in each of them. The latter was obtained by multiplying the area of a cell (0.25 m²) by the measured thickness. We also quantified the maximum error associated with the volume, which is linearly dependent on the standard deviation ($\sigma_{\Delta z} = 20$ cm) between the two DTMs [76]. To distinguish the thickness contribution from the lava and PDC deposits, we applied a cross-sectional approach [32,40] along the southern flow. We measured the elevation on the 2022 and 2023 DTMs and extrapolated the basal surface of the PDC deposit. Based on this analysis, and supported by field observations, we divided the pyroclastic deposits into two zones of homogeneous thickness and evaluated the related average values. Multiplying each thickness by the area of the corresponding zone and summing the two values obtained, we calculated the volume of the PDC deposit through the planimetric approach [75]. We estimate an error of 20% for this volume, which is the magnitude commonly associated with the planimetric approach [55]. Finally, the lava volume was evaluated by subtracting the volume of pyroclasts from that of the whole deposit. At the same time, the associated error was estimated by summing the errors of these two quantities.

2.5. Field Data and Sedimentological Analysis

To study and sample the volcanoclastic deposit that was first observed on 27 May, on 19 June, we performed a field survey along the middle portion of the southern lava flow, between 2970 and 2875 m. The lava flow and the PDC deposit were first distinguished by observing them from the 2002–2003 scoria cone (Figure 1). After considering the above observation, we decided on how to proceed with the sampling process. The coordinates of the samples and their macroscopic features were noted directly during fieldwork. Samples were analyzed at the sedimentological laboratory of INGV-OE. They were weighed and dry-sieved at 1 phi intervals down to 63 microns.

3. Results

3.1. Volcanic Tremor and Infrasound Signals

The numerous and evident temporal variations in the RMS values enable us to make inferences on the evolution of the 21 May 2023 eruption and to identify the most energetic phases of activity. During the paroxysm, the volcanic tremor showed important variations in its amplitude for about 5 h (Figure 2). The RMS values showed a modest and transient weak amplitude increase in the early morning hours. It preceded the onset of the phase of significant tremor increase, associated with the paroxysmal activity, by about 1 h. Starting from 05:00, a gradual and constant growth of the tremor amplitude marked the beginning of the entire increase cycle. At 05:40, a further and more decisive rise was recorded; this

trend becomes even more consistent shortly after 06:30 and allowed the first peak of the RMS series to be reached at around 07:00. This interval coincides with the phases of greatest energy. In the period of greatest amplitude, a second important phase was recorded between 09:00 and 09:40, in which the tremor energy reached the highest values. Subsequently, from the end of this latest increase, a very fast abatement of the tremor amplitude was observed until around 10:00, when it reached very low values that were clearly lower than those of the period preceding the eruption.

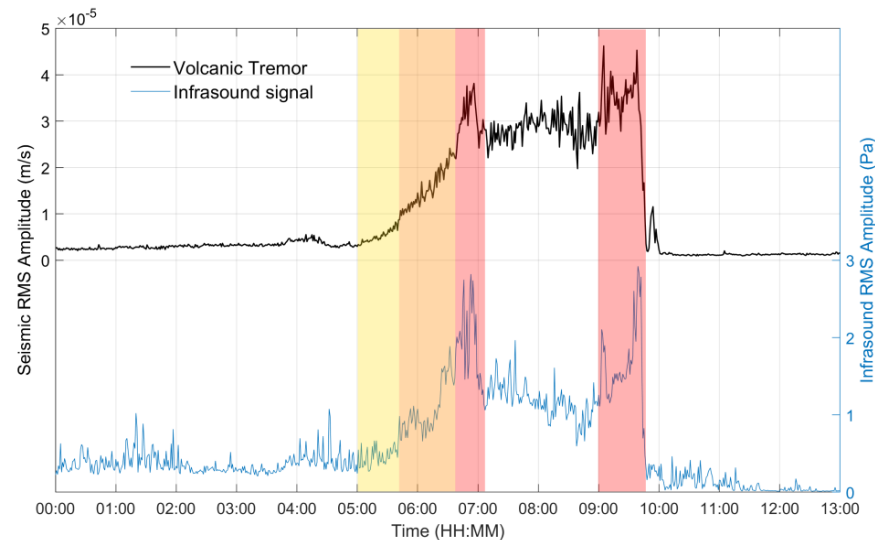


Figure 2. The upper portion of the figure shows, as a black line (left y -axis), the vertical component of the volcanic tremor; the lower portion shows, as a blue line (right y -axis), the infrasound RMS amplitudes from the ESLN station during the 21 May 2023 activity. The yellow and orange areas evidence the first gradual and the second decisive amplitude increases, respectively. The red areas point to the two most energetic phases.

In addition to the meteorological conditions during the studied period, which interfere with volcanogenic infrasound signals, the most energetic phases of the eruption were still traceable. Although the noise generated by wind prevents us from clearly identifying the onset of the amplitude increase, nevertheless, the first infrasound amplitude increase can be tracked from about 05:00. Successively, the infrasound time series resembles the seismic one. As in volcanic tremor RMS, infrasound signals exhibit two main energetic phases. At the end of the second one, their amplitude rapidly undergoes a decrease, probably marking the end of the eruption.

3.2. Radar Signals

The three analyzed radars were able to probe and quantitatively characterize the eruptive plume of the 21 May 2023 eruption, despite the weather cover that obstructed its visibility. The radar estimations of the H_{TP} (km) and the MER (kg/s) are shown in Figures 3 and 4, respectively. By analyzing the time trend of H_{TP} , we can identify the onset of the explosive activity at 05:50. The corresponding H_{TP} ranges between 4.2 km and 6.3 km, as detected by the radar in Catania (CT, magenta line) and Monte Lauro (ML, cyan line), whereas the radar in Reggio Calabria (RC, black line) did not detect this phase. This misalignment can be both due to the different viewpoints of the radars (Figure 1; RC is to the northeast of Etna, whereas CT and ML are to the south) and to the different possible occlusions of the volcanic plume due to the orography. All sensors match in detecting the two maximum explosive phases between 07:50 and 10:10, with an H_{TP} of 10–10.5 km (a.s.l.). We also observed an interbedded minimum in the activity at 08:50, probably related to a decrease in the lava fountain. Between 10:30 and 11:00, the RC radar detected an H_{TP} peak (2.9 km) lower than those of the other two radars (3.1 km and 5.1 km). The explosive activity ended at 12:00, as highlighted by the H_{TP} estimates of the ML and CT radars.

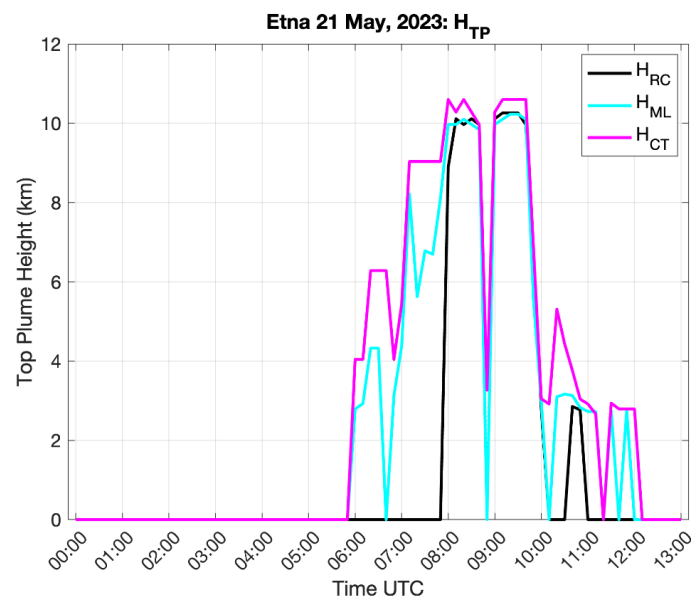


Figure 3. Etna explosive activity on 21 May 2023: time series of the top plume height (H_{TP} in km a.s.l.) derived by the radars at RC, ML, and CT (black, cyan, and magenta lines, respectively).

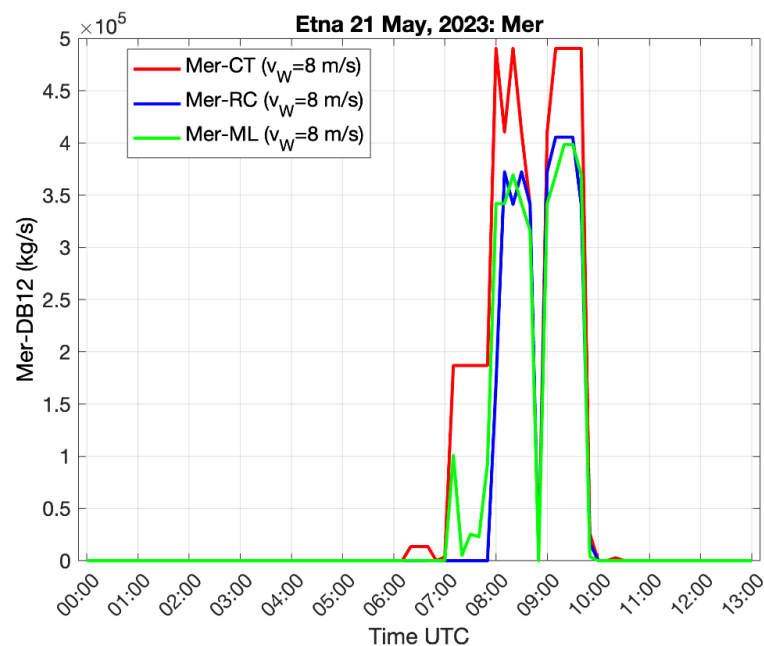


Figure 4. Etna explosive activity on 21 May 2023: time series of the MER (kg/s) computed by inputting the H_{TP} derived by the radars at CT, RC, and ML (red, blue, and green lines, respectively).

The retrieved sequences of the H_{TP} were used to train the DB12 model, assuming an average wind velocity of $v_W = 8$ m/s as derived by the ERA5 reanalysis for this time interval (06:00 to 12:00). Also in this analysis, all radars observed the maximum explosive phase between 07:50 and 10:10, when the MER reached the maximum value between 3.6×10^5 kg/s and 4.9×10^5 kg/s (Figure 3). The starting phase was around 07:00, when a lower MER value was observed, which then increased rapidly until 07:50. This time (07:00) confirms that estimated by analyzing the signal of the radar in CT. At 08:50, we observed a lowering of the MER estimates, similar to that observed for H_{TP} , which is the input for the DB12 model.

We overlapped the averaged H_{TP} derived from the radars at CT and ML with the time trend of the RMS of the volcanic tremor amplitude recorded by the ESLN station. However, we normalized the two quantities by their respective maximum values to obtain

comparable dimensionless ranges (Figure 5). From 05:50 to 10:00, the two signals show comparable trends, except between 06:30 and 06:40. In this interval, the normalized H_{TP} shows a decrease in contrast to the normalized RMS, which continues to increase. Then, from 06:40 to 09:50, both normalized signals show a good alignment.

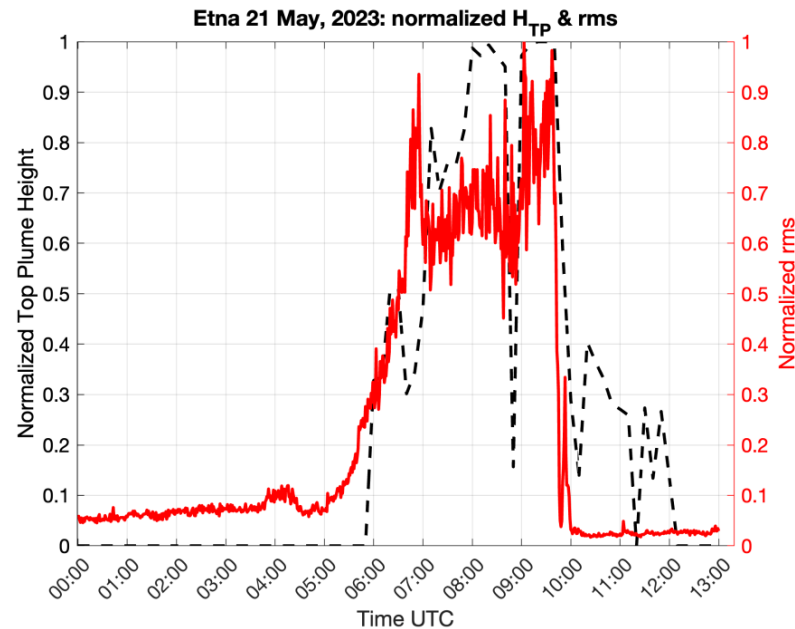


Figure 5. Time series of normalized HTP and normalized RMS tremor amplitude (dashed black and continuous red lines, respectively) are shown on the left and right axes, respectively.

3.3. Satellite Data

The Sentinel 3-A satellite passed over Etna on 21 May and scanned the scene between 09:27 and 09:30. From the OLCI dataset, we measured that the coldest pixel has a BT, at $10.85 \mu\text{m}$, of 219.08 K and a BTD of -0.18 K . By considering an error of approximately 10% (i.e., $\pm 2 \text{ K}$), as proposed in [72], the estimated plume altitude in the proximity of over the vent is $15.44 \pm 1.06 \text{ km}$. Figure 6a displays the eruption in RGB and the defined area in magenta. Figure 6b shows the temperature gradient with a purple line; the ± 2 temperature interval is in pink, and the coldest pixel is the light blue polka dot. The higher point is not considered because the maximum height reached by Etna volcanic plumes is about 15 km [77].

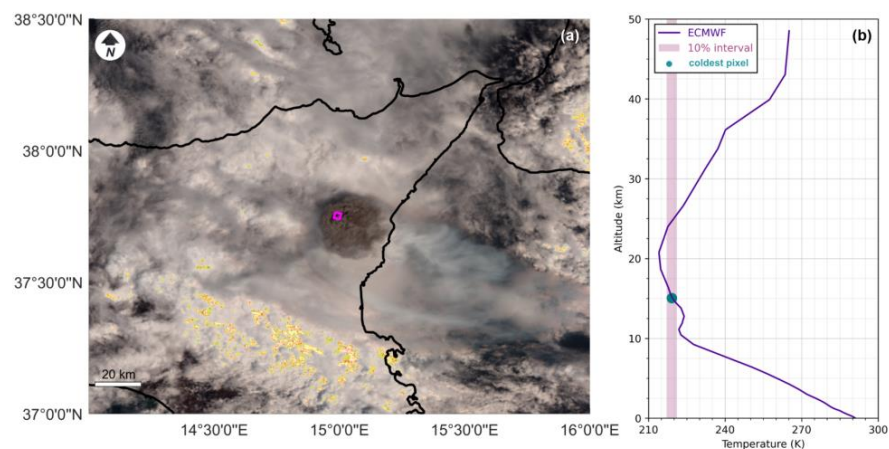


Figure 6. (a) The OLCI RGB image of 21 May 2023 at 09:27:35–09:30:35 shows the eruptive plume, and the fuchsia rectangle depicts the 2.7 km^2 area centered on Etna; (b) The temperature gradient, as a function of the altitude (km a.s.l.), is shown by the purple curve, the ± 2 temperature interval is in pink, and the coldest pixel at $10.85 \mu\text{m}$ is highlighted by the light blue polka dot.

3.4. UAS Data

The analysis of UAS-derived orthomosaics and DTMs enables the mapping of the two lava flows of the 21 May 2023 eruption and the PDCs to be distinguished from the underlying lava flow by their different colors—reddish and black, respectively (Figure 7A,B). The southern and eastern lava flows had minimum elevations of 2650 m and 2660 m and lengths of 2.3 km and 1.3 km, respectively. The PDC deposit was confined within the southern lava flow boundaries, and it extended down to 2740 m, with a run-out of 1.6 km. The thickness of the southern lava flow had an average and maximum value of 2.7 m and 10.7 m, respectively (Figure 7C). The tephra accumulated on the southern and southwestern flank of the SEC had an average and maximum thickness of 9.1 m and 24.3 m, respectively (Figure 7C). On the other hand, a lack of material, which corresponds to negative thickness values, was observed on the southern and southern–southeastern flanks of the SEC. The thickness of the PDC ranged from 1 m to 0.5 m in the upper and distal portions, respectively (Figure 7D,E). The SEC reached an ellipsoidal elevation of 3393 ± 4 m, which is almost the same as that of the previous year (3390 m). The resulting volumes were $(1.40 \pm 0.19) \times 10^6 \text{ m}^3$ for the southern flow, $(1.40 \pm 0.28) \times 10^5 \text{ m}^3$ for the eastern flow, and $(1.30 \pm 0.26) \times 10^5 \text{ m}^3$ for the PDC.

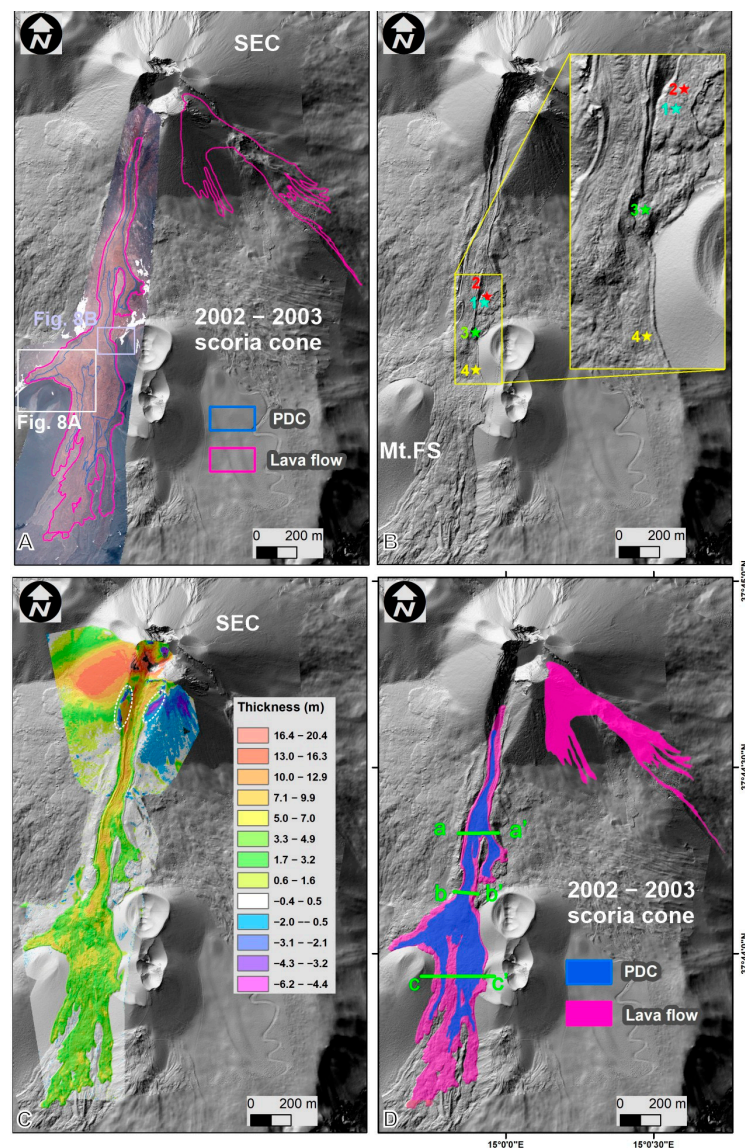


Figure 7. Cont.

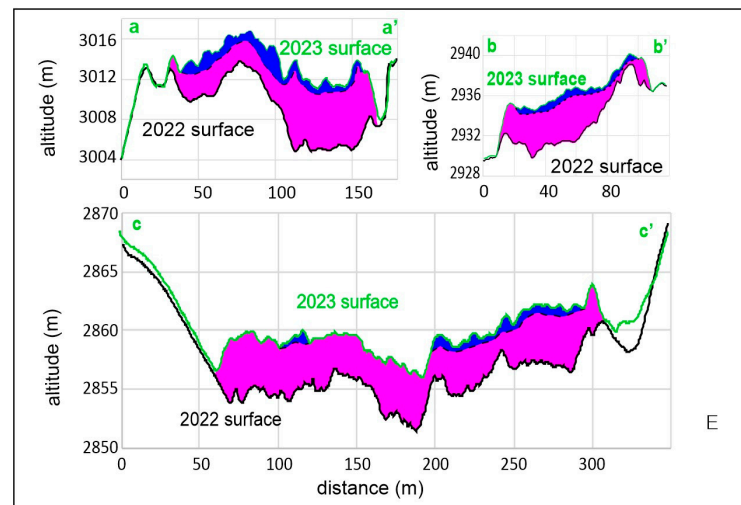


Figure 7. (A) Orthomosaic obtained from UAS surveys. (B) Shaded relief obtained from the 2023 DTM; stars indicate sample locations. (C) Differences between the 2022 and 2023 DTMs; elliptical white dotted lines envelop the area with a lack of material. (D) Geological map; the green lines indicate the cross-sectional location, whose endpoints are indicated by aa', bb' and cc'. (E) Cross sections showing the stratigraphic contact between the lava flow and the PDC deposit; the black dotted line indicates the deduced stratigraphic contact.

3.5. Field Data and Sedimentological Analysis

During the field surveys, we observed the lava flow extending southwards from the fissure of the SEC (Figure 8A), and a PDC deposit consisting of altered, reddish bombs to lapilli-size scoria above the southern lava flow (Figure 8A). The deposit had clear wave-like compression ridges on the surface produced during the downslope movement, the so-called ogives [78]. Blocks of sizes ranging from 0.4 to 2.0 m were distributed from 2900 and 3030 m a.s.l. They consisted of agglutinated red scoria (Figure 8B–D) and a scoriaceous bomb field associated with a ballistics trajectory south of the SEC up to about 1.5 km from the volcanic vent (Figure 8E). The four samples of the pyroclastic deposit were collected from its middle east portion (Figure 7B) and they had a median grain size, ranging from -5.3 to -4.6 phi, with a fine tail of coarse ash. The sorting ranged from 1 to 2.4 phi (Figure 9).

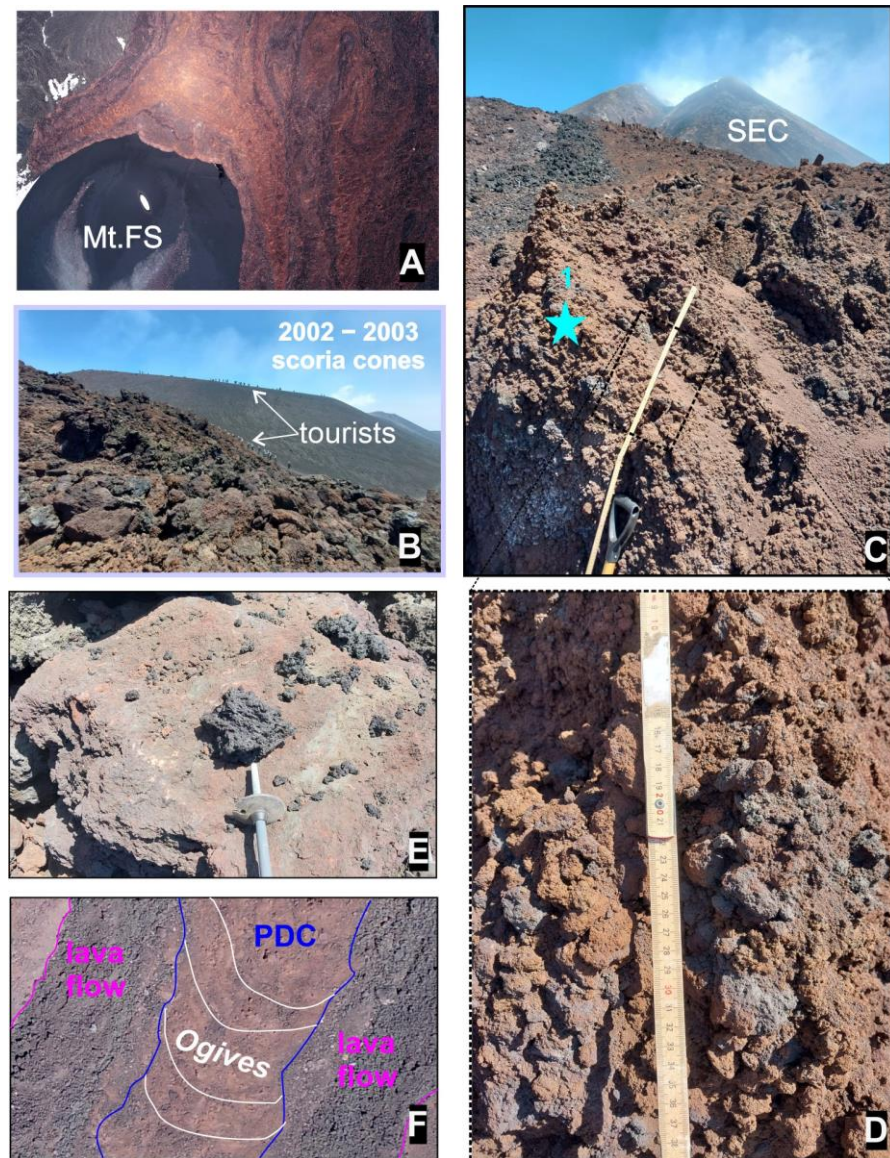


Figure 8. (A) The UAS image depicts the lava flow and the PDC deposit that have overlapped each other. The field images depict (B) the PDC deposit, the 2002–2003 scoria cones in the background, and the well-visible group of tourists above and below the cones (for location, see Figure 7A). (C) Sample 1 (the star indicates its location, see Figure 7B) and the SEC in the background. (D) Detailed view of (C). (E) Spatter of the 21 May lava fountain, located about 1.5 km from the vent. (F) Details of the ogives (highlighted by the white lines) on the PDC deposit.

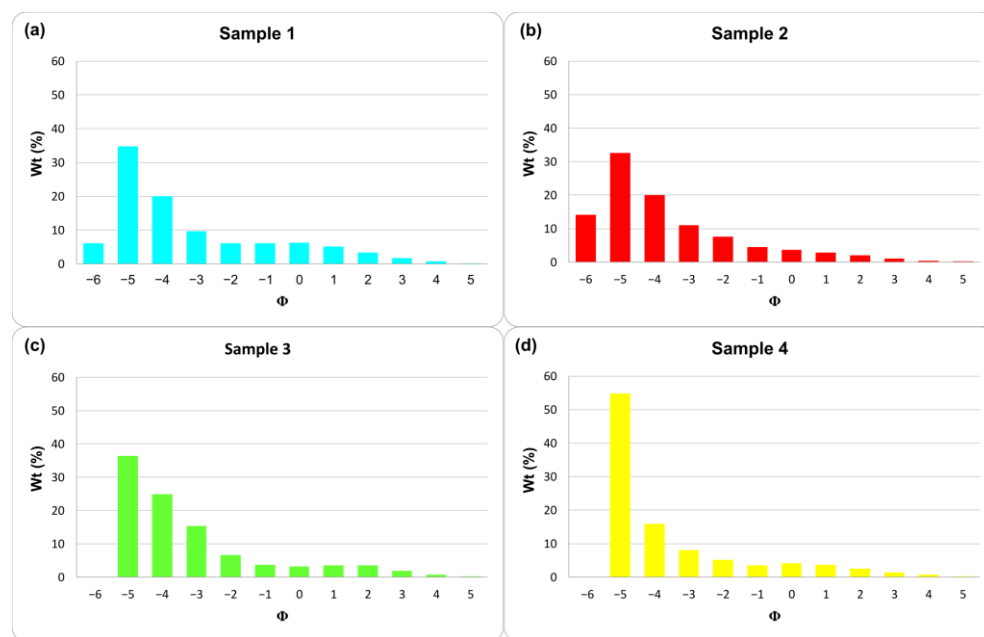


Figure 9. Grain-size distributions of the analyzed samples: (a) Sample 1; (b) Sample 2; (c) Sample 3; (d) Sample 4. The color of each graph is the same as that of the star locating the corresponding sample in Figure 7B.

4. Discussion

This work combines various geological, geophysical, and sedimentological investigations to characterize the 21 May 2023 hidden eruption of Etna that was not directly or remotely observed, given the poor weather conditions. This eruption produced lava flows and a PDC, which had not been observed before the survey we carried out on 27 May 2023. The observation of this PDC deposit prompted us to carefully analyze the event, using a variety of data including seismic, infrasound, and radar signals, satellite and UAS images, and samples collected during fieldwork.

The joint analysis of tremor and infrasound RMSs and maximum plume height allowed us to hypothesize the temporal evolution of the eruption. The RMSs suggest that during the resumption phase, from about 05:00, Strombolian activity was ongoing but too mild to be detected by the radars. The increase in the explosive phase was measured by radar signals from about 05:50 and is confirmed by the more decisive rise in the RMS starting from 05:40. This phase was probably characterized by stronger Strombolian activity; indeed, the mass eruption rate was still quite low until 07:00, and the maximum top plume height was about 6 km. Then, from 06:30 to 06:40, the height of the eruption column decreased while the volcanic tremor increased. We can suppose that this discrepancy could be due to intense Strombolian activity, a still unstable regime of the lava fountain, or the transition from the first to the latter phase. However, the lack of direct volcanological observations does not allow us to better explain the two different trends. From 06:40 to 09:50, both signals show a good alignment, probably coinciding with the lava fountain. Starting from 09:50 the tremor shows a very fast abatement that should coincide with the return to Strombolian activity. Finally, the re-establishment of the background tremor amplitude corresponds to the cessation of the eruptive episode [14]. This occurred at 10:00, when the mass eruption rate was close to zero. However, until 12:00, the top plume height was not zero, but was generally less than 3 km. This is due to the finest tephra that were still hanging around in the troposphere. From our analysis, we evaluate that the whole eruptive event and its paroxysmal phase lasted about 5 and 3 h, respectively. This paroxysm duration is comparable with the average duration (2.9 h) of the events of the first eruptive cycle of 2021 but is higher than that (1.6 h) of the second cycle of 2021 [40].

Seismic and infrasound signals recorded during the analyzed episode, both in the time and spectral domains, were also investigated by looking for potential signals associated with a PDC, and any significant transient was distinguished. In the literature, among the different PDCs that occurred at the Etna volcano, few have been analyzed from a seismic and infrasound point of view [79,80]. Only the PDC of 11 February 2014 gave evidence of these kinds of signals [61]. One hypothesis on the lack of seismic and infrasound signature is that the energetic signals related to the eruptive episode could have masked such a source. In particular, the signal of the PDC could be masked by both the very high amplitude and spectral content typical of lava fountains occurring at Etna [18], which would result in overlaps with that of the PDC ([61], and references therein). A second reason could be related to the characteristics of the PDC, such as the runout distance and volume, its direction, and, thus, the source–station distance. Indeed, it has to be said that the PDC of 11 February 2014 consisted of a volume three times higher than the studied one [61].

The analysis of radars and satellite data enables us to measure the 21 May 2023 column height as ranging between 10 and 15 km. This range is comparable to what was observed for Etna's recent lava fountains [77]. Moreover, starting from the instantaneous values of column height estimated by time steps of 10 min from the three radars, we obtain a total mass of pyroclasts within the volcanic plume that ranges between 2×10^9 kg and 9×10^9 kg. This value is in line with the tephra produced during Etna's lava fountains [77].

The analysis of UAS data allows us to quantify the lava flows and the PDC deposit of the 21 May 2023 paroxysm. The total volume of the two lava flows is $(1.54 \pm 0.47) \times 10^6$ m³ and is comparable with the average volume per event of the 2011–2014 and 2021 SEC paroxysms, which were 1.7×10^6 m³ and $(1.8 \pm 0.3) \times 10^6$ m³, respectively [40,81]. The volume of the PDC deposit is $(1.30 \pm 0.26) \times 10^5$ m³; considering this low value, it seems reasonable that the detachment niche was not detectable either from the ground or in remote surveys. Moreover, it was probably concealed by the spatter and bombs deposited in the proximal area, except for a small portion at the top of the scar that remained without any material deposition (Figure 8C). At Etna, in the last 20 years, four main collapses of the SEC have occurred, on 16 November 2006 [51], 11 February 2014 [53], and 10 and 21 February 2022 [82], and several minor PDCs occurred during 2021 paroxysms [83]. In the first two cases, flank collapses occurred at the eastern flank of the SEC, facing the Valle del Bove. This could be due to several fractures that weakened the flanks, which are essentially composed of unconsolidated material interbedded with lava flows on a high steep. In addition, the Valle del Bove, a deep depression with a horseshoe shape, triggers a gravitational pull on the SEC eastern flank. However, in February 2022 and on 21 May 2023, the PDCs were emplaced on the south flank, particularly above and around the 2002–2003 scoria cone. This is a guide's favorite area to bring tourists to admire the SEC, considering that it is only 800 m away from this observation point (Figure 8B). The previous cases were characterized by a runout distance of between 1.6 and 2.3 km and a volume of between 0.3 and 0.9×10^6 m³, which is at least three times higher than the material of the 21 May 2023 PDC ($0.13 \pm 0.026 \times 10^6$ m³). In the last decades, more attention has been devoted to the hazard posed by the potentially frequent flank failures of the composite cones on the Etna summit area. However, the only existing study for Etna on PDCs, which also includes a simulation but not a hazard map, dates back to 2006 [51].

The analysis of the samples collected in the field shows that they are mainly formed by coarse particles with a median grain size ranging from -5.3 to -4.6 phi and with a fine tail of coarse ash. Such size distributions are coarser than the distributions of samples collected on the deposit of the SEC flank collapse that occurred on 16 November 2006 [51]. The location of the 21 May 2023 samples, at a distance of 0.8 to 1.2 km from the vent, explains their coarser distribution.

5. Conclusions

On 21 May 2023, a terrible snowstorm concealed an eruption at the Etna Southeast Crater. By cross-referencing various data sources, including seismic, infrasonic, and radar surveillance

systems; fieldwork; and satellite and UAS images, we gained a better understanding of the event. This multidisciplinary approach allowed for detailed mapping, quantification, and characterization of the products, and an increased awareness of volcanic activities.

This paper emphasizes the advantages of using remote sensing monitoring systems, particularly in situations where visibility is limited, as well as the importance of fieldwork. Indeed, the UAS and ground surveys allowed the identification of a hazard that would otherwise have been overlooked, i.e., the occurrence of a PDC caused by a small partial collapse of the SEC. In general, our results show the potential multi-hazards associated with volcanic eruptions and the need for ongoing research to better understand their behavior.

Considering the number of visible and hidden flank collapses that have taken place in recent decades in Etna's summit area, we suggest the necessity of implementing updated PDC hazard maps that take into account Etna's current summit topography, which has changed dramatically in the last 15 years. Several hazard maps of lava flow invasion [84,85], tephra fallout [46,86], and the impact of large-size clasts and ballistics [49,50,77] have already been created for Etna. However, more needs to be done regarding PDC hazards, and this paper could be a step forward in that direction.

Author Contributions: Conceptualization, E.D.B., C.P. and S.S.; methodology, software, validation, formal analysis, investigation, resources, data curation, E.D.B., C.P., S.S., M.C., L.M., F.R., L.P., M.S. and S.A.; writing—original draft preparation, writing E.D.B. and C.P.; review and editing, E.D.B. and C.P.; visualization, E.D.B., C.P., S.S., M.C., L.M., F.R., L.P., M.S. and S.A.; supervision, E.D.B. and C.P.; project administration, E.D.B. and S.S.; funding acquisition, E.D.B. and S.S. All authors have read and agreed to the published version of the manuscript.

Funding: This work was supported by funding provided by the Italian Presidenza del Consiglio dei Ministri—Dipartimento della Protezione Civile (DPC), Convenzione Attuativa DPC-INGV, Accordo-Quadro Dipartimento della protezione civile—INGV 2022-2025, and by the INGV-MIUR project Pianeta Dinamico “Working Earth” sub-project VT—DYNAMO—2023 and sub-project SAFARI. This paper does not necessarily represent DPC's official opinion and policies. L. Pioli was funded by F73C23001610007 project sponsored by Fondazione di Sardegna.

Data Availability Statement: Images and analysis can be requested from the authors.

Acknowledgments: We would like to thank Daniele Pellegrino for his cooperation in a UAS survey, and the scientists and technicians from INGV-OE for maintaining the seismic monitoring network and the Sedimentology laboratory. We are grateful to the CETEMPS of L'Aquila University and the Italian Civil Protection Department (DPC) for the provision of the X-band radar data.

Conflicts of Interest: The authors declare no conflicts of interest. The funders had no role in the design of the study; in the collection, analyses, or interpretation of data; in the writing of the manuscript; or in the decision to publish the results.

References

1. Tilling, R.I. Introduction to special section on how volcanoes work: Part 1. *J. Geophys. Res.* **1987**, *92*, 13685–13686. [[CrossRef](#)]
2. Andronico, D.; Branca, S.; Calvari, S.; Burton, M.; Caltabiano, T.; Corsaro, R.A.; Del Carlo, P.; Garfi, G.; Lodato, L.; Miraglia, L.; et al. A multi-disciplinary study of the 2002–03 Etna eruption: Insights into a complex plumbing system. *Bull. Volcanol.* **2005**, *67*, 314–330. [[CrossRef](#)]
3. Corsaro, R.A.; Andronico, D.; Behncke, B.; Branca, S.; Caltabiano, T.; Ciancitto, F.; Cristaldi, A.; De Beni, E.; La Spina, A.; Lodato, L.; et al. Monitoring the December 2015 summit eruptions of Mt. Etna (Italy): Implications on eruptive dynamics. *J. Volcanol. Geotherm. Res.* **2017**, *341*, 53–69. [[CrossRef](#)]
4. Coppola, D.; Laiolo, M.; Cigolini, C.; Massimetti, F.; Delle Donne, D.; Ripepe, M.; Arias, H.; Barsotti, S.; Parra, C.B.; Centeno, G.R.; et al. Thermal remote sensing for global volcano monitoring: Experiences from the MIROVA system. *Front. Earth Sci.* **2020**, *7*, 362. [[CrossRef](#)]
5. Cannata, A.; Di Grazia, G.; Montalto, P.; Ferrari, F.; Nunnari, G.; Patanè, D.; Privitera, E. New insights into banded tremor from the 2008–2009 Mount Etna eruption. *J. Geophys. Res. Solid Earth* **2010**, *115*, B12318. [[CrossRef](#)]
6. Cannata, A.; Di Grazia, G.; Giuffrida, M.; Gresta, S.; Palano, M.; Sciotto, M.; Viccaro, M.; Zuccarello, F. Space-time evolution of magma storage and transfer at Mt. Etna volcano (Italy): The 2015–2016 reawakening of Voragine crater. *Geochem. Geophys. Geosyst.* **2018**, *19*, 471–495. [[CrossRef](#)]

7. Chouet, B.A.; Matoza, R.S. A multi-decadal view of seismic methods for detecting precursors of magma movement and eruption. *J. Volcanol. Geotherm. Res.* **2013**, *252*, 108–175. [[CrossRef](#)]
8. McNutt, S.R.; Nishimura, T. Volcanic tremor during eruptions: Temporal characteristics, scaling and constraints on conduit size and processes. *J. Volcanol. Geotherm. Res.* **2008**, *178*, 10–18. [[CrossRef](#)]
9. Viccaro, M.; Zuccarello, F.; Cannata, A.; Palano, M.; Gresta, S. How a complex basaltic volcanic system works: Constraints from integrating seismic, geodetic, and petrological data at Mount Etna volcano during the July–August 2014 eruption. *J. Geophys. Res. Solid Earth* **2016**, *121*, 5659–5678. [[CrossRef](#)]
10. Sparks, R.S.J.; Biggs, J.; Neuberg, J.W. Monitoring Volcanoes. *Science* **2012**, *335*, 1310–1311. [[CrossRef](#)]
11. Almendros, J.; Chouet, B.; Dawson, P. Spatial extent of a hydrothermal system at kilauea volcano, Hawaii, determined from array analyses of shallow long period seismicity: 2. Results. *J. Geophys. Res. Solid Earth* **2001**, *106*, 13581–13597. [[CrossRef](#)]
12. Patané, D.; Di Grazia, G.; Cannata, A.; Montalto, P.; Boschi, E. Shallow magma pathway geometry at Mt. Etna volcano. *Geochem. Geophys. Geosyst.* **2008**, *9*, 12. [[CrossRef](#)]
13. Viccaro, M.; Garozzo, I.; Cannata, A.; Di Grazia, G.; Gresta, S. Gas burst vs. gas-rich magma recharge: A multidisciplinary study to reveal factors controlling duration of the recent paroxysmal eruptions at Mt. Etna. *J. Volcanol. Geotherm. Res.* **2014**, *278–279*, 1–13. [[CrossRef](#)]
14. Alparone, S.; Andronico, D.; Lodato, L.; Sgroi, T. Relationship between tremor and volcanic activity during the Southeast Crater eruption on Mount Etna in early 2000. *J. Geophys. Res.* **2003**, *108*, 2241. [[CrossRef](#)]
15. Andronico, D.; Cannata, A.; Di Grazia, G.; Ferrari, F. The 1986–2021 paroxysmal episodes at the summit craters of Mt. Etna: Insights into volcano dynamics and hazard. *Earth Sci. Rev.* **2021**, *220*, 103686. [[CrossRef](#)]
16. Gresta, S.; Lombardo, G.; Cristofolini, R. Characteristics of volcanic tremor accompanying the September 24th, 1986 explosive eruption of Mt. Etna (Italy). *Ann. Geophys.* **1996**, *39*, 411–420. [[CrossRef](#)]
17. Alparone, S.; Andronico, D.; Sgroi, T.; Ferrari, F.; Lodato, L.; Reitano, D. Alert system to mitigate tephra fallout hazards at Mt. Etna Volcano, Italy. *Nat. Hazards* **2007**, *43*, 333–350. [[CrossRef](#)]
18. Cannata, A.; Catania, A.; Alparone, S.; Gresta, S. Volcanic tremor at Mt. Etna: Inferences on magma dynamics during effusive and explosive activity. *J. Volcanol. Geotherm. Res.* **2008**, *178*, 19–31. [[CrossRef](#)]
19. La Spina, A.L.; Burton, M.R.; Allard, P.; Alparone, S.; Muré, F. Open-path FTIR spectroscopy of magma degassing processes during eight lava fountains on Mount Etna. *Earth Planet. Sci. Lett.* **2015**, *413*, 123–134. [[CrossRef](#)]
20. Andronico, D.; Scollo, S.; Cristaldi, A.; Ferrari, F. Monitoring ash emission episodes at Mt. Etna: The 16 November 2006 case study. *J. Volcanol. Geotherm. Res.* **2009**, *180*, 123–134. [[CrossRef](#)]
21. Cannavò, F.; Sciotto, M.; Cannata, A.; Di Grazia, G. An integrated geophysical approach to track magma intrusion: The 2018 Christmas Eve eruption at Mt. Etna. *Geophys. Res. Lett.* **2019**, *46*. [[CrossRef](#)]
22. Matoza, R.; Fee, D.; Green, D.; Mialle, P. Volcano infrasound and the international monitoring system. In *Infrasound Monitoring for Atmospheric Studies*; Le Pichon, A., Blanc, E., Hauchecorne, A., Eds.; Springer: Berlin/Heidelberg, Germany, 2019; pp. 1023–1077.
23. Sciotto, M.; Watson, L.M.; Cannata, A.; Cantarero, M.; De Beni, E.; Johnson, J. Infrasonic gliding reflects a rising magma column at Mount Etna (Italy). *Sci. Rep.* **2022**, *12*, 16954. [[CrossRef](#)] [[PubMed](#)]
24. Allstadt, K.E.; Matoza, R.S.; Lockhart, A.B.; Moran, S.C.; Caplan-Auerbach, J.; Haney, M.M.; Thelen, W.A.; Malone, S.D. Seismic and acoustic signatures of surficial mass movements at volcanoes. *J. Volcanol. Geotherm. Res.* **2018**, *364*, 76–106. [[CrossRef](#)]
25. McNutt, S.R. Volcanic tremor and its use in estimating eruption parameters. In *Proceedings of the 2nd International Conference on Volcanic Ash and Aviation Safety*, Alexandria, VA, USA, 21–24 June 2004; Section 2. US Department of Commerce: Washington, DC, USA; NOAA: Washington, DC, USA, 2004; pp. 49–50.
26. Ripepe, M.; Bonadonna, C.; Folch, A.; Delle Donne, D.; Lacanna, G.; Marchetti, E.; Höskuldsson, A. Ash-plume dynamics and eruption source parameters by infrasound and thermal imagery: The 2010 Eyjafjallajökull eruption. *Earth Planet. Sci. Lett.* **2013**, *366*, 112–121. [[CrossRef](#)]
27. De Angelis, S.; Diaz-Moreno, A.; Zuccarello, L. Recent developments and applications of acoustic infrasound to monitor volcanic emissions. *Remote Sens.* **2019**, *11*, 1302. [[CrossRef](#)]
28. De Angelis, S.; Zuccarello, L.; Scollo, S.; Mereu, L. Assessment of eruption source parameters using infrasound and plume modelling: A case study from the 2021 eruption of Mt. Etna, Italy. *Sci. Rep.* **2023**, *13*, 19857. [[CrossRef](#)] [[PubMed](#)]
29. Marzano, F.S.; Mereu, L.; Montopoli, M.; Cimini, D.; Martucci, G. Volcanic ash cloud observation using ground-based Ka-band radar and near-infrared Lidar ceilometer during the Eyjafjallajökull eruption. *Ann. Geophys.* **2015**, *57*. [[CrossRef](#)]
30. MSG-SEVIRI. Available online: https://www.esa.int/esapub/bulletin/bullet111/chapter4_bul111.pdf (accessed on 4 April 2024).
31. Romeo, F.; Mereu, L.; Scollo, S.; Papa, M.; Corradini, S.; Merucci, L.; Marzano, F.S. Volcanic Cloud Detection and Retrieval Using Satellite Multisensor Observations. *Remote Sens.* **2023**, *15*, 888. [[CrossRef](#)]
32. De Beni, E.; Cantarero, M.; Neri, M.; Messina, A. Lava flows of Mt Etna, Italy: The 2019 eruption within the context of the last two decades (1999–2019). *J. Maps* **2021**, *17*, 65–76. [[CrossRef](#)]
33. Chevrel, M.O.; Villeneuve, N.; Grandin, R.; Froger, J.-L.; Coppola, D.; Massimetti, F.; Campus, A.; Hrysiewicz, A.; Peltier, A. Lava flow daily monitoring: The case of the 19 September–5 October 2022 eruption at Piton de la Fournaise. *Volcanica* **2023**, *6*, 391–404. [[CrossRef](#)]
34. Kauahikaua, J.; Poland, M. One hundred years of volcano monitoring in Hawaii. *Eos Trans. Am. Geophys. Union.* **2012**, *93*, 29–30. [[CrossRef](#)]

35. Turner, N.R.; Perroy, R.L.; Hon, K. Lava flow hazard prediction and monitoring with UAS: A case study from the 2014–2015 Pāhoā lava flow crisis, Hawaii ‘i. *J. Appl. Volcanol.* **2017**, *6*, 17. [[CrossRef](#)]
36. Genzano, N.; Marchese, F.; Plank, S.; Pergola, N. Monitoring the Mauna Loa (Hawaii) eruption of November–December 2022 from space: Results from goes-r, sentinel-2 and Landsat-8/9 observations. *Int. J. Appl. Earth Obs. Geoinf.* **2023**, *122*, 103388. [[CrossRef](#)]
37. Branca, S.; Del Carlo, P. Eruptions of Mt Etna during the past 3.200 years: A revised compilation integrating the Historical and stratigraphic records. In *Mount Etna Volcano Laboratory*; Bonaccorso, A., Calvari, S., Coltelli, M., Del Negro, C., Falsaperla, S., Eds.; Geophysical Monograph Series 143; American Geophysical Union: Washington, DC, USA, 2004; pp. 1–27.
38. Bombrun, M.; Spampinato, L.; Harris, A.; Barra, V.; Caltabiano, T. On the transition from Strombolian to fountaining activity: A thermal energy-based driver. *Bull. Volcanol.* **2016**, *78*, 15. [[CrossRef](#)]
39. Behncke, B.; Neri, M. Cycles and trends in the recent eruptive behaviour of Mount Etna (Italy). *Can. J. Earth Sci.* **2003**, *40*, 1405–1411. [[CrossRef](#)]
40. Proietti, C.; De Beni, E.; Cantarero, M.; Ricci, T.; Ganci, G. Rapid provision of maps and volcanological parameters: Quantification of the 2021 Etna volcano lava flows through the integration of multiple remote sensing techniques. *Bull. Volcanol.* **2023**, *85*, 58. [[CrossRef](#)]
41. Chester, D.K.; Duncan, A.M.; Guest, J.E.; Kilburn, C.R.J. *Mount Etna: The Anatomy of a Volcano*; Chapman and Hall: London, UK, 1985; p. 404.
42. Blong, R.J. *Volcanic Hazards: A Sourcebook on the Effects of Eruptions*. Academic Press: Sydney, Australia, 1984; p. 484.
43. Cioni, R.; Andronico, D.; Cappelli, L.; Aravena, A.; Gabellini, P.; Cristaldi, A.; Corsaro, R.A.; Cantarero, M.; Ciancitto, F.; De Beni, E.; et al. Products and dynamics of lava-snow explosions: The 16 March 2017 explosion at Mount Etna, Italy. *GSA Bulletin* **2023**. [[CrossRef](#)]
44. Amiridis, V.; Kampouri, A.; Gkikas, A.; Misios, S.; Gialitaki, A.; Marinou, E.; Rennie, M.; Benedetti, A.; Solomos, S.; Zanis, P.; et al. Aeolus winds impact on volcanic ash early warning systems for aviation. *Sci. Rep.* **2023**, *13*, 7531. [[CrossRef](#)]
45. Guffanti, M.; Ewert, J.W.; Gallina, G.M.; Bluth, G.J.S.; Swanson, G.L. Volcanic-ash hazard to aviation during the 2003–2004 eruptive activity of Anatahan volcano, Commonwealth of the Northern Mariana Islands. *J. Volcanol. Geotherm. Res.* **2005**, *146*, 241–255. [[CrossRef](#)]
46. Scollo, S.; Coltelli, M.; Bonadonna, C.; Carlo, P. Tephra hazard assessment at Mt. Etna (Italy). *Nat. Hazards Earth Syst. Sci.* **2013**, *13*, 3221–3233. [[CrossRef](#)]
47. Andronico, D.; Del Carlo, P. PM10 measurements in urban settlements after lava fountain episodes at Mt. Etna, Italy: Pilot test to assess volcanic ash hazard to human health. *Nat. Hazards Earth Syst. Sci.* **2016**, *16*, 29–40. [[CrossRef](#)]
48. Andronico, D.; Scollo, S.; Cristaldi, A. Unexpected hazards from tephra fallouts at Mt Etna: The 23 November 2013 lava fountain. *J. Volcanol. Geotherm. Res.* **2015**, *304*, 118–125. [[CrossRef](#)]
49. Osman, S.; Rossi, E.; Bonadonna, C.; Frischknecht, C.; Andronico, D.; Cioni, R.; Scollo, S. Exposure-based risk assessment and emergency management associated with the fallout of large clasts at Mount Etna. *Nat. Hazards Earth Syst. Sci.* **2019**, *19*, 589–19610. [[CrossRef](#)]
50. Costa, G.; Mereu, L.; Prestifilippo, M.; Scollo, S.; Viccaro, M. Modeling the trajectories of ballistics in the summit area of Mt. Etna (Italy) during the 2020–2022 sequence of lava fountains. *Geosciences* **2023**, *13*, 145. [[CrossRef](#)]
51. Norini, G.; De Beni, E.; Andronico, D.; Polacci, M.; Burton, M.; Zucca, F. The 16 November 2006 flank collapse of the south-east crater at Mount Etna, Italy: Study of the deposit and hazard assessment. *J. Geophys. Res.* **2009**, *114*, B02204. [[CrossRef](#)]
52. Behncke, B. Hazards from pyroclastic density currents at Mt. Etna (Italy). *J. Volcanol. Geotherm. Res.* **2009**, *180*, 148–160. [[CrossRef](#)]
53. Andronico, D.; Di Roberto, A.; De Beni, E.; Behncke, B.; Bertagnini, A.; Del Carlo, P.; Pompilio, M. Pyroclastic density currents at Etna volcano, Italy: The 11 February 2014 case study. *J. Volcanol. Geotherm. Res.* **2018**, *357*, 92–105. [[CrossRef](#)]
54. Jones, T.J.; Beckett, F.; Bernard, B.; Breard, E.C.P.; Dioguardi, F.; Dufek, J.; Engwell, S.; Eychenne, J. Physical properties of pyroclastic density currents: Relevance, challenges and future directions. *Front. Earth Sci.* **2023**, *11*, 1218645. [[CrossRef](#)]
55. Calvari, S.; Nunnari, G. Comparison between automated and manual detection of lava fountains from fixed monitoring thermal cameras at Etna Volcano Italy. *Remote Sens.* **2022**, *14*, 2392. [[CrossRef](#)]
56. Mereu, L.; Scollo, S.; Bonadonna, C.; Donnadieu, F.; Freret-Lorgeril, V.; Marzano, F.S. Ground-based remote sensing and uncertainty analysis of the mass eruption rate associated with the 3–5 December 2015 Paroxysms of Mt. Etna. *IEEE J. Sel. Top. Appl. Earth Obs. Remote Sens.* **2021**, *15*, 504–518. [[CrossRef](#)]
57. Alparone, S.; Bonforte, A.; Gambino, S.; Grassi, S.; Guglielmino, F.; Latino, F.; Morreale, G.; Patti, G.; Privitera, L.; Obrizzo, F.; et al. Characterization of an active fault through a multiparametric investigation: The Trecastagni Fault and its relationship with the dynamics of Mt. Etna volcano (Sicily, Italy). *Remote Sens.* **2022**, *14*, 19–4760. [[CrossRef](#)]
58. Bonaccorso, A.; Currenti, G.; Linde, A.; Sacks, S.; Sicali, A. Advances in understanding intrusive, explosive and effusive processes as revealed by the borehole dilatometer network on Mt. Etna Volcano. *Front. Earth Sci.* **2020**, *7*, 357. [[CrossRef](#)]
59. Bollettino Etna of 23 May 2023. Available online: <https://www.ct.ingv.it/index.php/monitoraggio-e-sorveglianza/prodotti-del-monitoraggio/bollettini-settimanali-multidisciplinari/779-bollettino-Settimanale-sul-monitoraggio-vulcanico-geochimico-e-sismico-del-vulcano-Etna-del-2023-05-23/file> (accessed on 28 February 2024).
60. G.R.A.S. Sound and Vibration. G.R.A.S. 40an 1/2" ext. Polarized Free-Field Microphone, Low Frequency, Specification Sheet. Available online: <https://pdf.directindustry.com/pdf/gras-sound-vibration/gras-40an-1-2-ext-polarized-free-field-microphone-low-frequency/70183-402157.html> (accessed on 22 April 2024).

61. Watson, L.M.; Cannata, A.; Andronico, D. Tracking a pyroclastic density current with seismic signals at Mt. Etna (Italy). *J. Geophys. Res. Solid Earth* **2023**, *128*, e2022JB026114. [[CrossRef](#)]
62. Marzano, F.S.; Picciotti, E.; Vulpiani, G.; Montopoli, M. Synthetic signatures of volcanic ash cloud particles from X-band dual-polarization radar. *IEEE Trans. Geosci. Remote Sens.* **2012**, *20*, 193–211. [[CrossRef](#)]
63. Mereu, L.; Marzano, F.S.; Montopoli, M.; Bonadonna, C. Retrieval of tephra size spectra and mass flow rate from C-band radar during the 2010 Eyjafjallajökull eruption, Iceland. *IEEE Trans. Geosci. Remote Sens.* **2015**, *53*, 5644–5660. [[CrossRef](#)]
64. Marzano, F.S.; Mereu, L.; Scollo, S.; Donnadieu, F.; Bonadonna, C. Tephra mass eruption rate from ground-based X-band and L-band micro-wave radars during the 23 November 2013, Etna Paroxysm. *IEEE Trans. Geosci. Remote Sens. Inst. Electr. Electron. Eng.* **2020**, *58*, 1–14. [[CrossRef](#)]
65. Mereu, L.; Scollo, S.; Bonadonna, C.; Freret-Lorgeril, V.; Marzano, F.S. Multisensor characterization of the incandescent jet region of lava fountain-fed tephra plumes. *Remote Sens.* **2020**, *12*, 3629. [[CrossRef](#)]
66. European Centre for Medium-Range Weather Forecasts. Available online: <https://cds.climate.copernicus.eu/cdsapp#!/home> (accessed on 28 February 2024).
67. Degruyter, W.; Bonadonna, C. Improving on mass flow rate estimates of volcanic eruptions. *Geophys. Res. Lett.* **2012**, *39*, 16308. [[CrossRef](#)]
68. Mereu, L.; Scollo, S.; Garcia, A.; Sandri, L.; Bonadonna, C.; Marzano, F.S. A new radar-based statistical model to quantify mass eruption rate of volcanic plumes. *Geophys. Res. Lett.* **2023**, *50*, e2022GL100596. [[CrossRef](#)]
69. Bourg, L.; Bruniquel, J.; Henocq, C.; Morris, H.; Dash, J.; Preusker, R.; Dransfeld, S. Copernicus Sentinel-3 OLCI Land User Handbook, 1.2. Available online: <https://sentinel.esa.int/documents/247904/4598066/Sentinel-3-OLCI-Land-Handbook.pdf> (accessed on 28 February 2024).
70. Bourg, L.; Bruniquel, J.; Henocq, C.; Morris, H.; Dash, J.; Preusker, R.; Dransfeld, S. Copernicus Sentinel-3 SLSTR Land User Handbook, 1.3. Available online: <https://sentinel.esa.int/documents/247904/4598082/Sentinel-3-SLSTR-Land-Handbook.pdf> (accessed on 28 February 2024).
71. EUMETSAT Data Store. Available online: <https://data.eumetsat.int/search?query=#> (accessed on 28 February 2024).
72. Prata, A.J.; Grant, I.F. Retrieval of Microphysical and Morphological Properties of Volcanic Ash Plumes from Satellite Data: Application to Mt Ruapehu, New Zealand. *Q. J. R. Meteorol. Soc.* **2001**, *127*, 2153–2179. [[CrossRef](#)]
73. Agisoft Metashape. Available online: <https://www.agisoft.com> (accessed on 28 February 2024).
74. Cloud Compare. Available online: <https://www.cloudcompare.org/> (accessed on 28 February 2024).
75. Stevens, N.F.; Wadge, G.; Murray, J.B. Lava flow volume and morphology from digitised contour maps: A case study at Mount Etna, Sicily. *Geomorphology* **1999**, *28*, 251–261. [[CrossRef](#)]
76. De Beni, E.; Cantarero, M.; Messina, A. UAVs for volcano monitoring: A new approach applied on an active lava flow on Mt. Etna (Italy), during the 27 February–2 March 2017 eruption. *J. Volcanol. Geotherm. Res.* **2019**, *369*, 250–262. [[CrossRef](#)]
77. Scollo, S.; Prestifilippo, M.; Bonadonna, C.; Cioni, R.; Corradini, S.; Degruyter, W.; Rossi, E.; Silvestri, M.; Biale, E.; Carparelli, G. Near-Real-Time Tephra Fallout Assessment at Mt. Etna, Italy. *Remote Sens.* **2019**, *11*, 2987. [[CrossRef](#)]
78. Francis, P.; Oppenheimer, C. *Volcanoes*, 2nd ed.; Oxford University Press: New York, NY, USA, 2004; pp. 157–158.
79. Behncke, B.; Falsaperla, S.; Pecora, E. Complex magma dynamics at Mount Etna revealed by seismic, thermal, and volcanological data. *J. Geophys. Res.* **2009**, *114*, B0321. [[CrossRef](#)]
80. Sciotto, M.; Cannata, A.; Di Grazia, G.; Gresta, S.; Privitera, E.; Spina, L. Seismoacoustic investigations of paroxysmal activity at Mt. Etna volcano: New insights into the 16 November 2006 eruption. *J. Geophys. Res.* **2011**, *116*, B09301. [[CrossRef](#)]
81. De Beni, E.; Behncke, B.; Branca, S.; Nicolosi, I.; Carluccio, R.; D’Ajello Caracciolo, F.; Chiappini, M. The continuing story of Etna’s New Southeast Crater (2012–2014): Evolution and volume calculations based on field surveys and aero-photogrammetry. *J. Volcanol. Geotherm. Res.* **2015**, *303*, 175–186. [[CrossRef](#)]
82. Bollettini Settimanali Etna. Available online: [https://www.ct.ingv.it/index.php/monitoraggio-e-sorveglianza/prodotti-del-monitoraggio/bollettini-settimanali-multidisciplinari?filter\[search\]=etna](https://www.ct.ingv.it/index.php/monitoraggio-e-sorveglianza/prodotti-del-monitoraggio/bollettini-settimanali-multidisciplinari?filter[search]=etna) (accessed on 28 February 2024).
83. Pioli, L.; Pili, S.; Pili, V.; Scollo, S.; De Beni, E.; Cantarero, M. Integrating field and monitoring data for hazard assessment: An Etna type case. In Proceedings of the IUGG, Berlin, Germany, 11–20 July 2023.
84. Del Negro, C.; Cappello, A.; Neri, M.; Bilotta, G.; Hérault, A.; Ganci, G. Lava flow hazards at Mount Etna: Constraints imposed by eruptive history and numerical simulations. *Sci. Rep.* **2013**, *3*, 3493. [[CrossRef](#)] [[PubMed](#)]
85. Zuccarello, F.; Bilotta, G.; Ganci, G.; Proietti, C.; Cappello, A. Assessing impending hazards from summit eruptions: The new probabilistic map for lava flow inundation at Mt. Etna. *Sci. Rep.* **2023**, *13*, 19543. [[CrossRef](#)]
86. Pardini, F.; de Michieli Vitturi, M.; Andronico, D.; Esposti Ongaro, T.; Cristaldi, A.; Neri, A. Real-time probabilistic assessment of volcanic hazard for tephra dispersal and fallout at Mt. Etna: The 2021 lava fountain episodes. *Bull. Volcanol.* **2022**, *85*, 6. [[CrossRef](#)]

Disclaimer/Publisher’s Note: The statements, opinions and data contained in all publications are solely those of the individual author(s) and contributor(s) and not of MDPI and/or the editor(s). MDPI and/or the editor(s) disclaim responsibility for any injury to people or property resulting from any ideas, methods, instructions or products referred to in the content.